Enhancing densification in binder jet additive manufacturing of magnesium via nanoparticles as sintering aids

Mojtaba SALEHI[1*], Kai Xiang KUAH[1,2], Zihan HUANG[1,2], Daniel John BLACKWOOD[1], Su Xia ZHANG[1], Hang Li SEET[1], Mui Ling Sharon NAI[1**].

[1]Additive Manufacturing Division, Singapore Institute of Manufacturing Technology (SIMTech), Agency for Science, Technology and Research (A*STAR), 5 Cleantech Loop, 636732, Singapore

[2]Department of Materials Science and Engineering, National University of Singapore, 9 Engineering Drive 1, 117575, Singapore

* Mojtaba_salehi@simtech.a-star.edu.sg

** Mlnai@simtech.a-star.edu.sg

Abstract

Additive manufacturing technologies for magnesium alloys have been developing faster than before, but many challenges are on the horizon. The native oxide film covering each Mg powder particle remains a significant challenge to overcome for further advancing sinter-based AM of Mg alloys. The present study investigated if, and how, adding calcium-containing sintering aids can push the sintering boundaries of binder-jet printed Mg powder towards a faster densification rate. Calcium-containing nanoparticles were mixed with Mg-Zn-Zr powder to prepare feedstock for binder jetting and sintering. The as-printed and as-sintered samples were investigated using various characterization methods, including scanning electron microscopy, vibrational spectroscopy, density measurement, chemical analysis, and mechanical tests. The results showed that adding the sintering aid to Mg powder improved its densification rate by up to 25%. Compared to the monolithic Mg counterpart, the physical and mechanical properties of the Mg-0.2 wt.% Ca sample increased (i.e., the relative density ~7%, tensile strength ~30%, compressive strength ~15%, elastic modulus ~18%, and elongation

~185%). These improvements are discussed in the context of consumption mechanisms of calcium interacting with the Mg powder, its MgO film, and the other alloying elements. The current study has taken the first step towards developing a targeted nano-alloying approach to enhance the printing and post-printing processes for Mg alloys fabricated by binder jetting and fused filament fabrication.

Keywords: Additive manufacturing; binder jetting; magnesium; sintering

1. Introduction

Magnesium (Mg) is the lightest metal that possesses adequate mechanical properties for structural applications while being biodegradable. These characteristics make Mg an attractive candidate for weight-critical structural and biomedical applications. The properties of pure Mg are often enhanced through either alloying [1, 2] and/or the incorporation of micron or nano-sized particles [3, 4], typically achieved via the conventional mixing-melting-casting processes [5]. These processes significantly improve the mechanical and/or the corrosion properties of resultant Mg-based materials for real-world applications.

Additive manufacturing (AM) has been attracting ever-increasing attention worldwide and becoming a game-changer technology in multiple industries. The advantages of AM lie not only in design freedom to overcome the limitations of traditional manufacturing technologies (i.e., subtractive and formative) but also in pushing the boundaries of what is possible in material properties [6]. Accordingly, advancing AM will broaden Mg's uses to many more applications. Although researchers have attempted to develop various AM technologies for Mg alloys (e.g., laser powder bed fusion [7], wire arc AM [8], friction stir-based AM [9], binder jetting [10-15], fused filament fabrication [16], and indirect 3D printing [17]), Mg is one of the most challenging metals to handle in AM technologies. This is because of Mg's inherent properties, such as a high affinity to oxygen, high reactivity, and low boiling point. Indeed, to the best of our knowledge, Mg is not listed among the available materials for AM by

commercial companies. The latest state-of-the-art on research activities about Mg-AM is reviewed elsewhere [18].

Native oxide films covering each Mg powder particle pose several challenges in powder-based AM of Mg alloys. The MgO film has a ~10 nm thickness and inevitably forms on the surface of each Mg powder particle [19]. This thickness keeps growing during the storage, handling, and processing of Mg powder, even in an inert atmosphere [20]. In laser powder bed fusion, the beam breaks the MgO film, and the resulting oxide inclusions disrupt the melt pool due to a lack of wettability with molten Mg metal. These oxide inclusions are ultimately left behind in the microstructure and adversely affect the performance of fabricated parts, especially corrosion properties [7, 21, 22]. In sinter-based AM of Mg alloys, the as-printed Mg part is composed of a loose packing of primary powder particles. The native oxide film in the as-printed condition remains intact or thickens from the interactions between the binder materials and Mg powder. Given the very low diffusivity of Mg atoms in MgO (i.e., $\sim 1.2 \times 10^{-42}$ m^2s^{-1} at 189 °C), solid state sintering of the as-printed Mg part is unfeasible [14]. Salehi et al. [14, 15] successfully used super-solidus liquid phase sintering to break the oxide film in as-printed ZK60 Mg powder, allowing faster mass transport among particles. Dong et al. [16] then employed this sintering method in extrusion-based printed Mg scaffolds. Afterwards, Su et al. [23] conducted complete liquid phase sintering to densify binder jet-printed small pellets of AZ91 powder. On the one hand, maintaining shape fidelity in the liquid phase sintering process, particularly for geometrically large parts with increasing shape complexity, strictly limits the maximum-allowable liquid fraction [24]. On the other hand, the liquid content directly relates to the sintering kinetics of as-printed Mg powder [15]. These two considerations result in a densification-shape fidelity trade-off dilemma, as reported by Salehi et al. [12, 14].

An alternative way to disrupt the oxide film is to use an element with more affinity to oxygen than Mg. Such elements could be calcium, yttrium, and beryllium. Wolff et al. [25]

mixed pure Mg powder with three types of Ca-containing powder (i.e., CaH_2, Ca-18 wt.% Mg, and Mg-7 wt.% Ca) to prepare a feedstock composition of Mg-1 wt.% Ca for conventional die-pressing and sintering. Their results indicated that adding Ca decreased the porosity from 15% to 2% and, in turn, increased compressive strength by up to 52%. One may argue that this improvement partially originated from breaking the oxide layer by the exerted mechanical force during powder compaction. While the argument is not addressed, this Ca-assisted sintering method has been employed in the metal injection moulding of Mg-Ca mixtures [26, 27]. The major concerns about this sintering method are the limited choice of chemical composition and the microstructural homogeneity.

We hypothesize that if nano-sized sintering aids were added to Mg powder, the required amount for the sintering aids would reduce, and their dispersion would be enhanced. As a result, the undesirable change in chemical composition would be minimized, and the resulting microstructure would be more homogenous. The present study aimed to investigate if and how the addition of Ca-containing nanoparticles as a sintering aid enhances the sintering densification rate of binder-jet printed Mg-Zn-Zr powder feedstock. Firstly, the binder jet printability of the Mg-Ca feedstock was assessed. Secondly, the characteristics of sintered Mg-Ca samples in terms of density, chemical composition, microstructure, tensile, and compression results were thoroughly evaluated and compared with the monolithic Mg counterpart.

2. Experimental procedure

2.1. Powder feedstock

Spherical ZK60 alloy powder (International Laboratory, USA) with the chemical composition of Mg-5.49 wt.% Zn-0.17 wt.% Zr and an average particle size of ~60 μm was used as the starting Mg powder. Ca-based ceramic nanoparticles with an average particle size of ~60 nm were prepared to mix with the Mg powder and make a nanocomposite feedstock for

binder jetting. The feedstock of Mg-0.2 wt.% Ca-containing nanoparticles was then prepared by mechanical mixing of the raw powders. Prior to mixing, the Mg powder, the nanoparticles, and Zirconia balls (to aid in dispersion) were placed in a bottle and sealed in a glove box. The bottle was mixed for 2 h at room temperature using an Inversina Tumbler Mixer at a speed of 50 rpm. Fig. 1 shows the SEM micrographs of the mechanically mixed Mg-0.2 wt.% Ca feedstock, indicating that the nanoparticles adhere to the Mg powder surface as a result of electrostatic and van der Waals' forces [28]. This adhesion ensures a desirable propensity of the nanocomposite feedstock to form a uniform particulate mixture within each spread-out layer during the binder jetting build process.

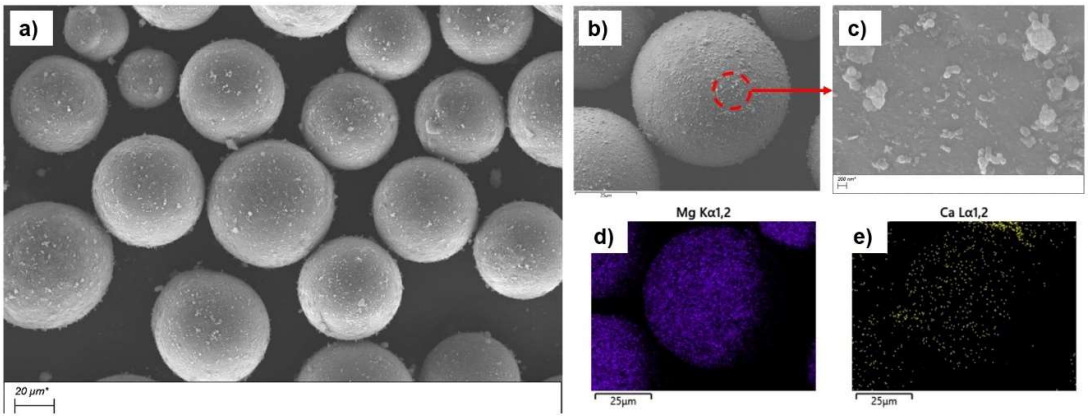

Fig. 1. Mg powder mixed with 0.2 wt.% Ca-containing nanoparticles. a-c) SEM micrographs, d) element mapping of (b) for Mg, and e) element mapping of (b) for Ca.

2.2. Binder jetting

The binder jetting and sintering of Mg feedstock have already been described elsewhere [12-15]. Briefly, the nanocomposite and monolithic Mg feedstock, hereafter denoted as Mg-Ca and Mg feedstock, were used to binder jet print green samples via an in-house modified 3D printer. Formulated ink was deposited on succeeding stacked layers of powder feedstock, each with a thickness of 100 µm, at a 70% saturation level. Afterward, the green samples were removed from the unbound powder in a build platform. They were placed in crucibles with a tight closing lid to sinter at 615 °C in a horizontal tube furnace in an argon atmosphere. Fig. 2 displays green samples with several geometries which were printed and sintered to perform

various material characterizations. The geometries include cylindrical pellets with 15 mm in diameter and 15 mm in height, cylinders with a diameter of 15 mm or 12 mm and a height of 95 mm, and cubes of dimension 15 mm.

Fig. 2. Pictorial representations of binder jet printed Mg-0.2 wt.% Ca samples. a) as printed, and b) as sintered

2.3. Characterization methods

The density of the Mg-Ca and Mg powder feedstock was measured using the gas pycnometer method (Micromeritics AccuPyc 1340), according to ASTM B923-22. The density of green samples was determined from the mass ratio to each sample volume. An analytical scale (0.01 mg resolution) and a digital caliper (0.01 mm resolution) were used to measure mass and dimension, respectively. The measurements were performed on six cubic samples. The Archimedes method was used to determine the density of sintered samples per ASTM B962. At least five specimens were tested to ensure data reproducibility. The oxygen content of the powder feedstocks and samples in as-printed and sintered conditions were measured by inert gas fusion-infrared absorbance (Eltra ONH 2000).

The powder feedstocks, as printed, and sintered samples were investigated using XRD (Bruker D8 Discover), with Cu K_α source. The samples were scanned theta-2-theta, with a 0.1° interval. The vibrational spectroscopy of as-printed samples was obtained using Fourier transform-infrared spectroscopy (FTIR) by placing a piece of the green sample on the diamond attenuated total reflection (ATR) crystal (Bruker Vertex 80v vacuum spectrometer). In

addition, Raman spectra were collected from the as-printed samples with laser source of λ = 514 nm (Renishaw InVia Raman Microscope).

The powder feedstocks, as printed, and sintered samples were examined using field-emission scanning electron microscopy (Zeiss EVO-50) equipped with energy dispersive X-ray spectroscopy (EDS). The SEM imaging and EDS analysis were performed with an accelerating voltage of 15–20 keV. For microstructural characterization, sintered samples were cut and their surface was ground and polished systematically to OPS (0.05 μm). The fine grinding and polishing were conducted by using an alcohol-based lubricant (DP-Lubricant Yellow, Struers), given Mg's sensitivity to aqueous-based solutions. The cross-section of sintered samples was analyzed by optical microscopy (Leica DM4000M Optical Microscope). In addition, Electron Backscatter Diffraction (EBSD, ZEISS Ultra Plus equipped with Oxford Symmetry S2) was carried out on the sintered samples. The sample surface was prepared via argon milling using a cross-section polisher (JEOL IB-19500CP). The EBSD was conducted with an accelerating voltage of 25 keV and resolution up to 0.1 μm.

The impulse excitation technique was used to calculate Young's modulus of sintered samples (RFDA, IMCE, Belgium). This test was performed on cylindrical specimens with a height of 60 mm and a diameter of 10 mm, according to ASTM E1876-15. The mechanical behaviour of sintered samples was evaluated under compression and tension loadings (Instron 5982) in accordance with ASTM E9-09 and ASTM E8/E8M-22, respectively. Five specimens with 8 mm in diameter and 12 mm in height were compressed. Three round specimens with a gauge length of 24 mm and a gauge diameter of 6 mm were machined from as-sintered cylindrical rods and pulled out. Finally, the fracture surface of tensile specimens was characterized using SEM.

3. Results and discussion

3.1. Characterization of binder jet-printed green samples

3.1.1. Microstructure

The homogenous distribution of Ca-containing nanoparticles provides Mg particles with uniform spatial distributions of Ca at a sintering temperature to reduce the MgO film. Fig. 3a shows a low-magnification SEM image of the green Mg-0.2 wt.% Ca sample. An interdigitate network of interparticle bridges formed among adjacent Mg particles. These bridges were derived from the interaction between the dispensing liquid binder and the superficial layer of Mg particles, mainly the native MgO film covering each Mg particle. The capillary force transfers the liquid and by-products of binder-Mg interactions to the interparticle bridges. This liquid flow stops when the liquid on the surface of connecting particles either drains or disrupts. Fig. 3b displays an exemplary pendular bridge formed in the green Mg-0.2 wt.% Ca sample. Fig. 3c and d show that some Ca-containing nanoparticles adhered to the surface of Mg particles while the others transferred to the interparticle bridges. Magnesium carbonate trihydrate (nesquehonite) with the chemical formula of $MgCO_3 \cdot 3H2O$, also formed in the solid interparticle bridges. This carbonate formed from the binder-Mg powder interactions, which was thoroughly investigated in binder jetting of Mg powder feedstock in our earlier studies [12, 13].

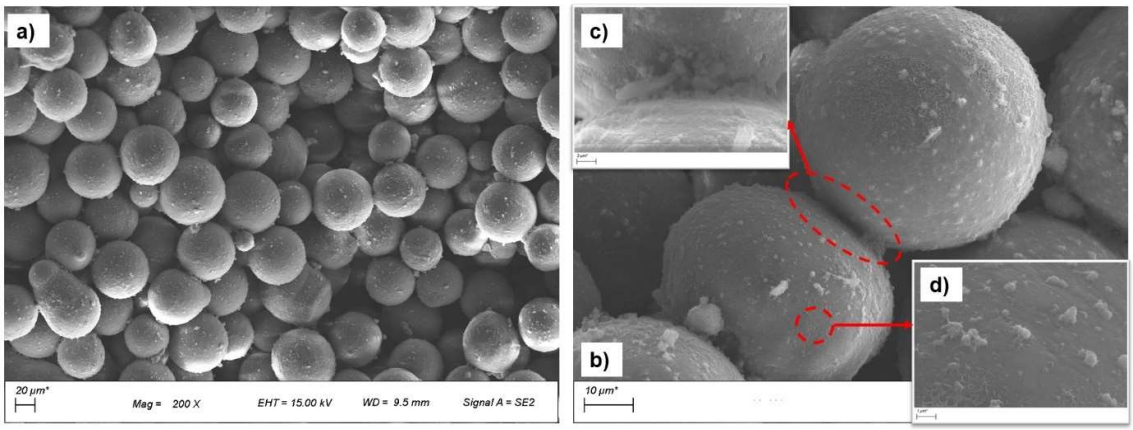

Fig. 3. The SEM micrographs of the Mg-0.2 wt.% Ca sample in the as-printed condition. a) formation of solid interparticle bridges among adjacent Mg particles derived from capillary-mediated bridging, b) an exemplary pendular bridge between Mg particles, c) a high magnification image of the solid interparticle bridge, and d) a high magnification image of the particle surface far from the bridge.

3.1.2. Interactions between the sintering aid and binder

The protection of sintering aids against the interaction with a liquid binder during binder jetting is of paramount importance. This retention is extremely challenging, given the high reactivity of Ca. Fig. 4 shows the X-ray diffractions collected from the Mg and Mg-0.2 wt.% Ca feedstocks in the as-received, as-mixed, and as-printed conditions. These patterns were identical, and no new peak was detected in the green Mg-0.2 wt.% Ca sample. Because of this absence, the samples were analyzed using vibrational spectroscopy due to their high sensitivity in identifying minute chemical changes. In our previous studies [12, 13], the vibrational spectroscopy results, together with microscopy and thermal analyses, indicated that MgH_2, $Mg(OH)_2$, MgO, and $MgCO_3 \cdot 3H_2O$ formed as a result of the interactions between the binder and pure Mg or Mg-Zn-Zr powder. Fig. 5 presents FTIR and Raman spectra of the green Mg-0.2 wt.% Ca sample. $Mg(OH)_2$ exhibited its characteristic FTIR O-H stretching band at 3697 cm^{-1} [29]. FTIR bands at around 3605, 1515, 1461, and 1382 cm^{-1} are consistent with $MgCO_3 \cdot 3H_2O$ [30, 31]. MgH_2 has a broad flattop band from 1000 to 1300 cm-1, centered at 1160 cm^{-1} [32]. The FTIR bands at 1160, 954, and 675 cm^{-1} confirm the presence of MgH_2 [33, 34]. The peak at 437 cm^{-1} corresponds to MgO [35]. The remaining bands represent the Ca-containing nanoparticles. The characteristic Raman band at 435 cm^{-1} is consistent with $Mg(OH)_2$ [36]. MgO exhibits its Raman band at 358 cm^{-1} and 618 cm^{-1} [37]. The Raman shift for $MgCO_3 \cdot 3H_2O$ is the band around 870 cm^{-1} [38]. MgH_2 exhibits strong Raman bands near 157 cm^{-1} and 1265 cm^{-1} [39, 40]. The remaining Raman bands correspond to the Ca-containing nanoparticles. Overall, these FTIR and Raman results confirmed that the nanoparticle sintering aid remained intact during binder jetting of the green Mg-0.2 wt.% Ca sample.

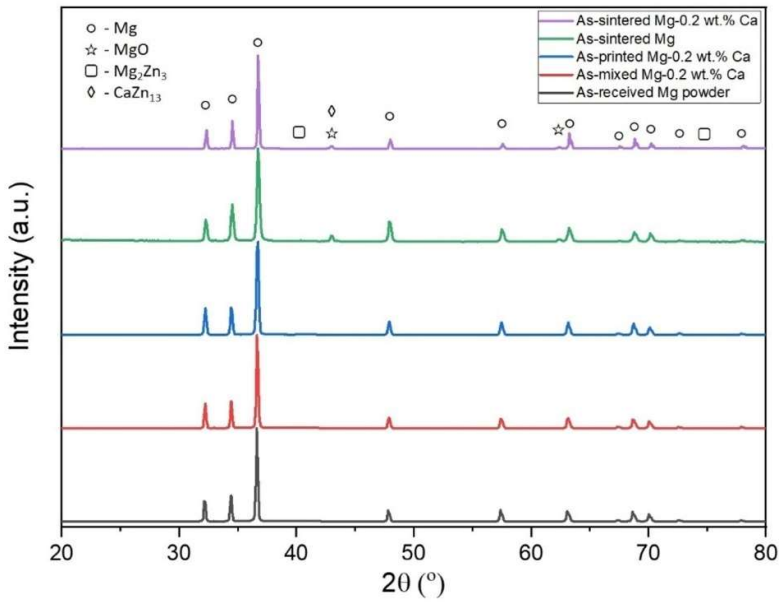

Fig. 4. XRD diffractograms of Mg and Mg-0.2 wt.% Ca powder feedstock in various conditions, namely, as-received, as-mixed, as-printed, and as-sintered.

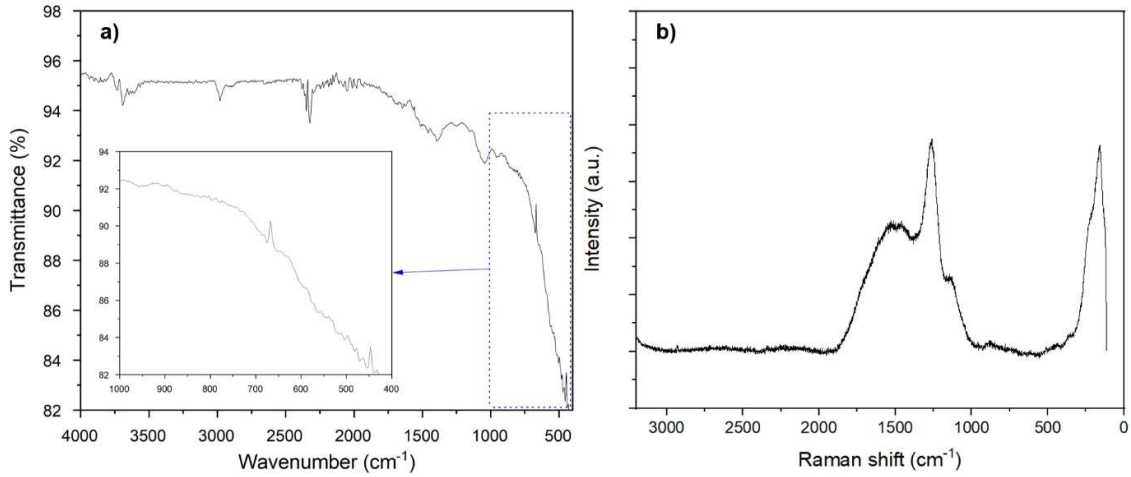

Fig. 5. Vibrational spectroscopy of the Mg-0.2 wt.% Ca sample in the as-printed condition. a) FTIR spectrum and b) Raman spectrum.

3.1.3. Density

The density of Mg-0.2 wt.% Ca and Mg samples in the as-printed condition was measured at 1.01 ± 0.01 g·cm^{-3} and 1.01 ± 0.02 g·cm^{-3}, respectively. The pycnometer density for the Mg-0.2 wt.% Ca and Mg powder feedstock were measured at 1.85 g·cm^{-3} and 1.83 g·cm^{-3}, respectively. With these pycnometer values as a denominator, the corresponding relative densities were calculated as 54.8 ± 0.7 for the green Mg-0.2 wt.% Ca sample and 55 ± 1 for the green Mg sample. These relative density values signify that the interparticle forces and packing

density of Mg-0.2 wt.% Ca feedstock are slightly affected. Generally, in binder jetting, the as-printed density is between the apparent density and the tapped density of a powder feedstock. The as-printed density determines the coordination number of particles in contact. This number plays a crucial role in the kinetics of a subsequent sintering process. Hence, it is essential for a sintering aid not to reduce the as-printed density by disrupting the interparticle forces acting among a particulate mixture in the feedstock.

We investigated if and how an increase in the nanoparticle content influences the as-printed density. We prepared two feedstocks of Mg-0.7 wt.% Ca and Mg-1.3 wt.% Ca, printed them, and measured their green density, as summarized in Table 1. The results showed a decreasing trend in the as-printed density (i.e., up to 11%) with increasing sintering aid content. In particular, the as-printed density reduced to 50.6 ± 0.8 and 49.0 ± 0.9 for the Mg-0.7 wt.% Ca and Mg-1.3 wt.% Ca samples, respectively. The impact of this density reduction on sintering is discussed in Section 3.2.1.

Table 1- Relative density of as-printed and as-sintered Mg alloys containing various amounts of Ca.

Specimens	Relative density (%)		Densification rate
	As printed	As sintered	
Mg	55 ± 1	86.8 ± 0.3	0.57
Mg-0.2 wt.% Ca	54.8 ± 0.7	93.5 ± 0.6	0.71
Mg-0.7 wt.% Ca	50.6 ± 0.8	87.0 ± 0.6	0.72
Mg-1.3 wt.% Ca	49.0 ± 0.9	80.7 ± 0.7	0.64

3.2. Characterization of binder-jet printed and sintered samples

3.2.1. Density

Table 1 summarizes the relative density of Mg with various Ca contents in the as-sintered condition. The maximum relative density of 93.5% was achieved in the Mg-0.2 wt.% Ca sample. The results showed that the relative density increased by 6.7% in the Mg-0.2 wt.% Ca sample compared to the Mg sample. The sintered density remained the same in the Mg-0.7 wt.% Ca and then decreased with a further increase of the sintering aid to 1.3 wt.% Ca. As discussed in Section 3.1.3, the as-printed density showed the decreasing trend with the sintering

aid contents. The densification rate, which defines as Eq.1, is used to study how adding the sintering aid affects the densification of Mg powder [24]:

$$\Delta\rho = (\rho - \rho_0) / \rho_0$$

Where $\Delta\rho$ is the densification rate, ρ is the sintered density, and ρ_0 is the as-printed density. Table 1 lists these values calculated for various samples. As expected, adding the sintering aid, irrespective of its quantity, enhanced the densification rate compared to the monolithic Mg counterpart. Interestingly, the densification rate is similar for the Mg-0.2 wt.% Ca and Mg-0.7 wt.% Ca samples, indicating up to 25% improvement in the density increment than that of the Mg sample. With the addition of Ca to 1.3 wt.%, the sintering aid efficacy reduced when compared to the range of 0.2 wt.% Ca to 0.7 wt.% Ca. This reduction could be originated from the lower as-printed density of Mg-1.3 wt.% Ca.

The distance between Mg powder particles is larger for a sample with a lower as-printed density. During the subsequent consolidation of as-printed samples by super-solidus liquid phase sintering, adjacent Mg particles must be connected via forming liquid bridges. In the case of an as-printed sample with a lower density, it is more likely that the interparticle spacing is too large for the effective formation of the liquid bridges, limited by both the amount of liquid phase and capillary effect. Capillary stress is the main driving force for the liquid phase sintering process—a greater capillary pressure results in higher densification [41]. Liu et al. [42] found an inverse relationship between the distance between neighbouring particles and the capillary pressure in liquid phase sintering. Accordingly, the capillary pressure during sintering the Mg-1.3 wt.% Ca sample would be smaller when compared to the Mg-0.2 wt.% Ca and Mg-0.7 wt.% Ca samples. As such, the sintering kinetics and, in turn, the densification rate would be lower for the Mg-1.3 wt.% Ca sample (Table 1).

3.2.2. Chemical composition

Given the results in Table 1, we selected the sintered Mg and Mg-0.2 wt.% Ca samples for further characterization. Table 2 displays the chemical compositions of the as-received Mg powder and the sintered Mg and Mg-0.2 wt.% Ca samples. As can be seen, the oxygen pick-up during the whole binder jetting and sintering processes is negligible, which is in line with our previous study on compositionally zero-sum binder jetting of Mg alloys [13]. Results in Table 2 indicated that the amounts of Zn and Zr elements in the sintered samples slightly deviate from the initial contents in the as-received powder. This process-induced compositional change stems from the evaporation of Mg and Zn elements during the liquid phase sintering process due to their low boiling temperatures (boiling point of Zn: 907 °C and Mg: 1091 °C). A compositional change during a manufacturing process is generally regarded as unfavourable. Indeed, this elemental evaporation is inevitable during the processing of Mg alloys such that the higher the processing temperature and time, the more significant the compositional change. In this regard, Kuah et al. [21] reported a 1% loss of Zn content in the Mg-Zn-Zr powder sintered at 573 °C, whereas the Zn loss increased to 6% for the sintered powder at 615 °C. Shuai et al. [43] and Wei et al. [44] observed 22% and 18% loss of Zn content in Mg-Zn-Zr powder processed by laser powder bed fusion. In addition, the elemental evaporation phenomenon during the laser-powder-bed fusion process could adversely affect the melt pool's stability [45].

Table 2- The chemical composition of the Mg powder in the as-received condition along with the Mg and Mg-0.2 wt.% Ca samples after binder jet printing and sintering.

Specimens	Zn (wt.%)	Zr (wt.%)	O (wt.%)	Ca (wt.%)	Mg (wt.%)
Mg powder in the as-received condition	5.49	0.17	0.02	0	Bal.
Binder jet printed and sintered Mg powder	5.33	0.24	0.03	0	Bal.
Binder jet printed and sintered Mg-0.2 wt.% Ca powder	5.26	0.22	0.01	0.19	Bal.

3.2.3. Microstructure

Fig. 6 shows optical micrographs of the Mg and Mg-0.2 wt.% Ca samples in the as-sintered condition. Fig. 7 displays the SEM micrographs of these samples. As seen from the optical micrographs and low magnification SEM images (Fig. 7a and c), a larger sinter neck diameter and, in turn, a denser microstructure with lower porosity were achieved in the Mg-0.2 wt.% Ca sample. These observations align with the higher Archimedes density of the Mg-0.2 wt.% Ca sample. A comparison between Fig. 7b and 7c shows that the lesser and thinner oxide layer covers each Mg powder particle in the Mg-0.2 wt.% Ca sample. This observation is supported by the EDS element mappings of the two samples, as depicted in Fig. 8 and 9. Taking the maps for Ca, O, and Mg into account, Ca and O co-exist in some areas near the surface of Mg particles, as indicated by the red arrows. In contrast, Mg is absent in those areas. This indicates that a fraction of Ca reacted with the native MgO film covering Mg particles. As a result, CaO replaced the MgO film on the particles' surface. More importantly, the Ca map for the Mg-0.2 wt.% Ca sample showed that Ca diffuses through the Mg powder particles. EDS point analyses determined the average chemical composition within the particles to be Mg-6.1 wt.% Zn- 0.2 wt.% Zr- 0.1 wt.% Ca.

Fig. 10 presents element maps of the selected regions at the grain boundaries of the Mg-0.2 wt.% Ca sample. In addition to MgO particles, Zn and Ca-rich precipitates were observed along the grain boundaries. EDS point analyses on the Zn and Ca-rich areas indicated that these precipitations were $CaZn_{13}$. This phase was also detected in the XRD pattern of the Mg-0.2 wt.% Ca sample (Fig. 4). The phase diagram of Ca-Zn showed a limited solubility of Ca in Zn. According to their binary phase diagram, $CaZn_{13}$ is the richest in terms of Zn content among all possible intermetallic phases between Ca and Zn elements. Moreover, multiple intermetallic phases are possible when considering the ternary phase diagram of Mg-Ca-Zn alloys [46]. The formation mechanism for the $CaZn_{13}$ intermetallic in Mg-Ca-Zn systems involves the

following transformations. According to theoretical calculations [46], $CaZn_{11}$ is first precipitated from a liquid phase at 805 K (Eq. 2). This phase then further reacts with the liquid phase constituent to precipitate $CaZn_{13}$ at 790 K (Eq. 3). Experimental studies found that $CaZn_{13}$ precipitates above 873 K (i.e., 600 ^{o}C) [47]. Given the sintering temperature of the Mg-0.2 wt.% Ca sample (i.e., 615 °C), the $CaZn_{13}$ precipitations were formed during the sintering process. As seen in Eq. 3, $MgZn_2$ precipitates together with the $CaZn_{13}$ intermetallic. $MgZn_2$ further reacts with the liquid to form Mg_2Zn_3 intermetallics at a temperature above 410 °C (Eq. 4) [46]. The XRD result (Fig. 4) and EDS analyses confirm the presence of Mg_2Zn_3 precipitations in the Mg and Mg-0.2 wt.% Ca samples.

$$L \leftrightarrow MgZn_2 + CaZn_{11} \quad (2)$$

$$L + CaZn_{11} \leftrightarrow MgZn_2 + CaZn_{13} \quad (3)$$

$$L + MgZn_2 \leftrightarrow Mg_2Zn_3 \quad (4)$$

Fig. 11a and b depict the EBSD images of Mg and Mg-0.2 wt.% Ca samples in Euler color mapping. Each color in the EBSD images represents individual grains, and areas in black color are pores. For both samples, two types of grains can be distinguished, namely, the circular-shaped grains and the irregular-shaped grains. The circular grains originated from the primary Mg powder and are smaller than the irregular grains. These circular grains have a grain size similar to the particle size of the starting Mg powder depending on where the observed grain was cross-sectioned. The irregular grains appear to be formed by the coalescence of adjacent Mg powder particles during the sintering process. These grains underwent a recrystallization process in view of their texture orientations. The EBSD results were statistically analyzed for the grain size measurements. For the sintered Mg sample, the grain sizes were in the range of 13.3 μm to 88.3 μm, and the average grain size was 41.4 ± 15.4 μm. For the Mg-0.2 wt.% Ca, the grain size ranged from 13.1 μm to 116.4 μm with an average of 47.3 ± 21.4 μm. The slightly larger grain size in the Mg-0.2 wt.% Ca sample could be associated with reducing more MgO

film in this sample. The lesser and thinner MgO film covering Mg powder particles allows more grains to coalesce and grow as sintering time progresses.

Table 3 summarizes the grain sizes of Mg alloys obtained in various fabrication methods. Comparisons of these sizes indicated that the grain sizes achieved in this study are close to those from metal injection molding (i.e., 23 μm); smaller than those achieved in conventional casting (i.e., 55–84 μm) and binder jetting consolidated by complete liquid phase sintering (i.e., 179–698 μm); and larger than those found in powder bed fusion melting (i.e., 7.3 μm). The results thus show that binder jetting creates an Mg part with a homogeneous microstructure, no residual stress, isotropic property, and microstructure independent of geometry. These advantages lie in the nature of the binder jetting process in stacking up layers of powder without exerting external mechanical loading to form a homogenous as-printed part. This part subsequently undergoes a homogeneous heating and cooling process of sintering to transform into a functional Mg part. This microstructural evolution contrasts with the fusion-based AM processes of Mg alloys, during which microstructure inhomogeneities are often induced due to consecutive melting and solidification steps. In wire-arc AM of Mg alloys, localized heating and cooling gradients cause various microstructures to form in different locations of fabricated parts [8]. Similarly, rapid solidification in laser powder bed fusion generates metastable microstructures with different textures and precipitations, which may diminish the mechanical and corrosion properties of fabricated Mg parts [31,32].

Fig. 11c shows a high magnification region of the Mg sample, focusing on the grain boundaries. The corresponding elemental mappings are depicted in Fig. 11d. Zn-rich secondary phase (i.e., Mg_2Zn_3) and MgO were observed to accumulate along the grain boundaries. Fig. 11e shows a high magnification region for the Mg-0.2 wt.% Ca sample near the grain boundaries, and the corresponding elemental mappings are shown in Fig. 11f. Considering the Zn, Ca, and O maps, several intermetallic and oxide compounds, namely, Mg_2Zn_3, $CaZn_{13}$,

MgO, and CaO were accumulated along the grain boundaries. These phases were present in the XRD pattern of the as-sintered Mg-0.2 wt.% Ca sample (Fig. 4). Statistical analysis of EBSD results indicated that the average surface area of MgO phase existing in the Mg-0.2 wt.% Ca sample was 80% lower than that presented in the Mg sample. This observation is consistent with the results of SEM and EDS element mappings (Fig. 7–9), indicating the lesser and thinner oxide in the Mg-0.2 wt.% Ca sample.

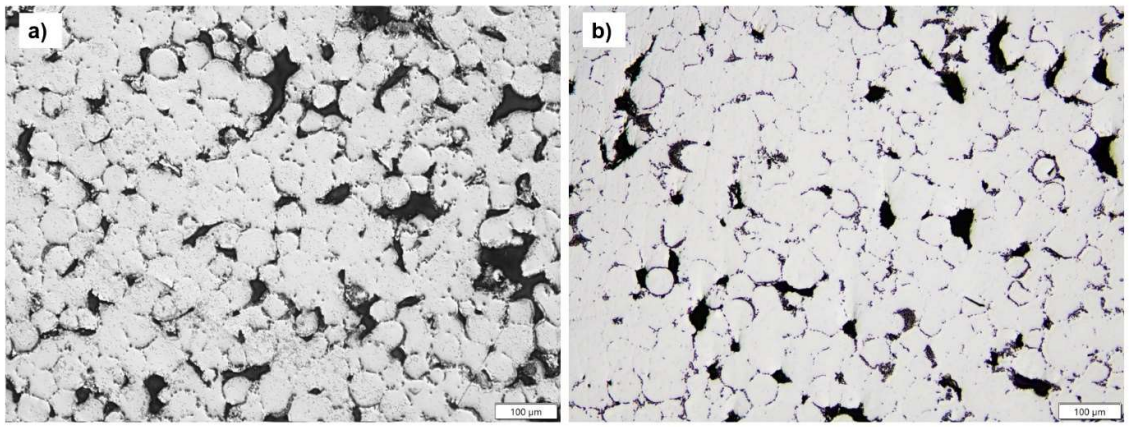

Fig. 6. The optical micrographs of binder jet printed and sintered samples, a) Mg and b) Mg-0.2 wt.% Ca.

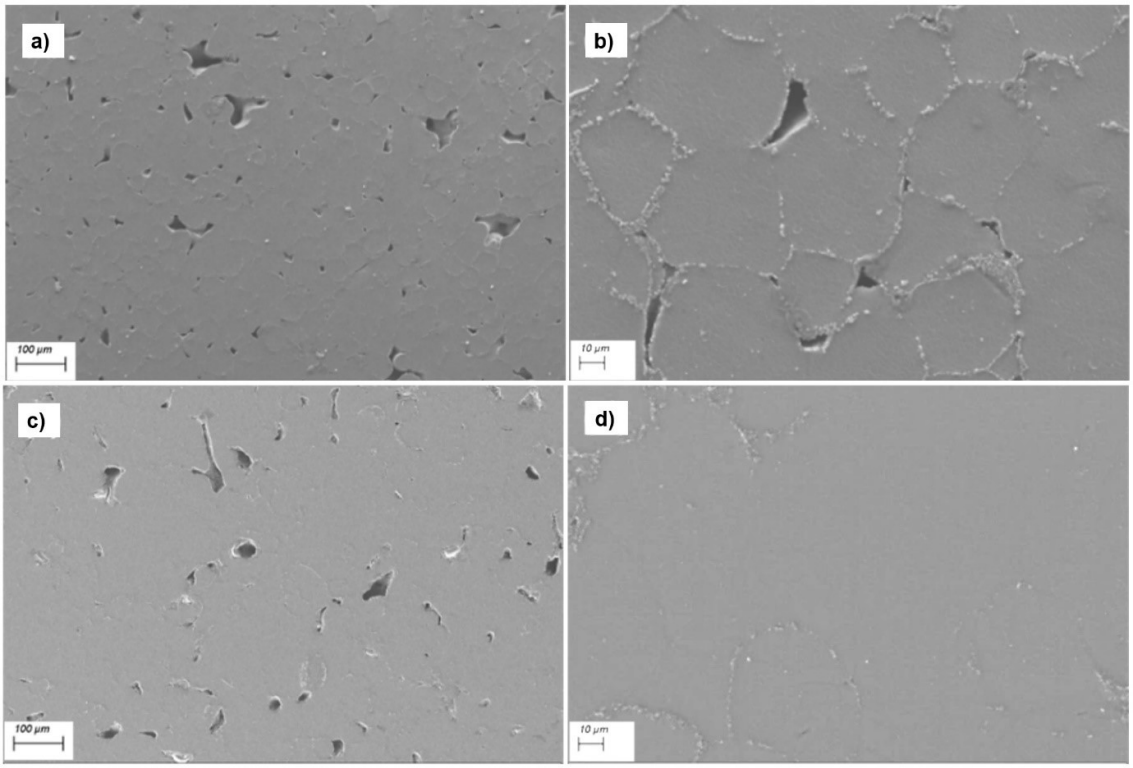

Fig. 7. The SEM micrographs of binder jet printed and sintered samples. a & b) Mg and c & d) Mg-0.2 wt.% Ca.

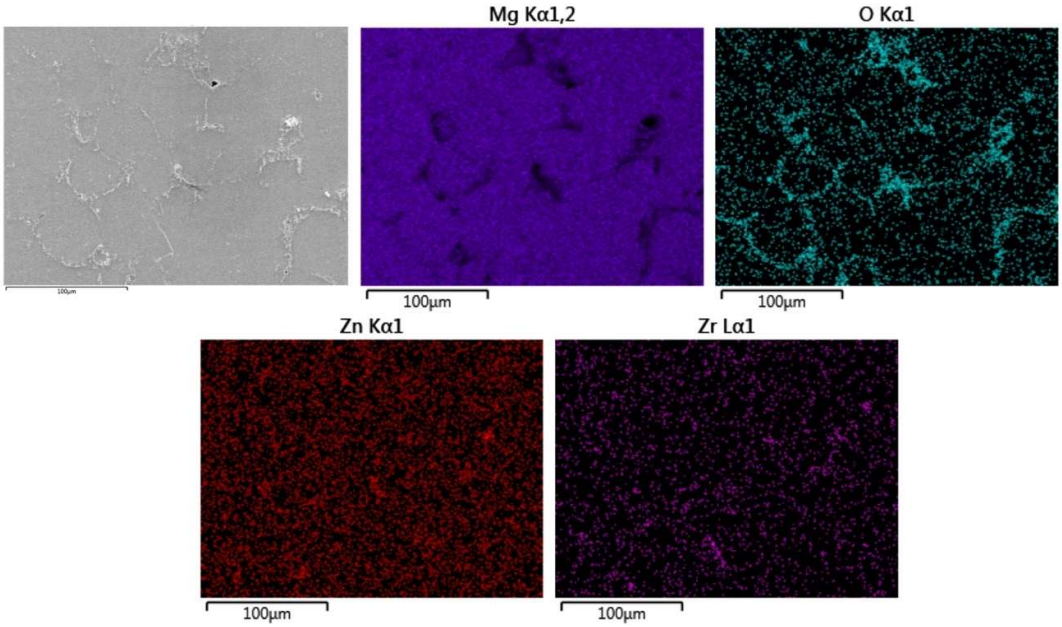

Fig. 8. EDS element mappings of binder jet printed and sintered Mg sample.

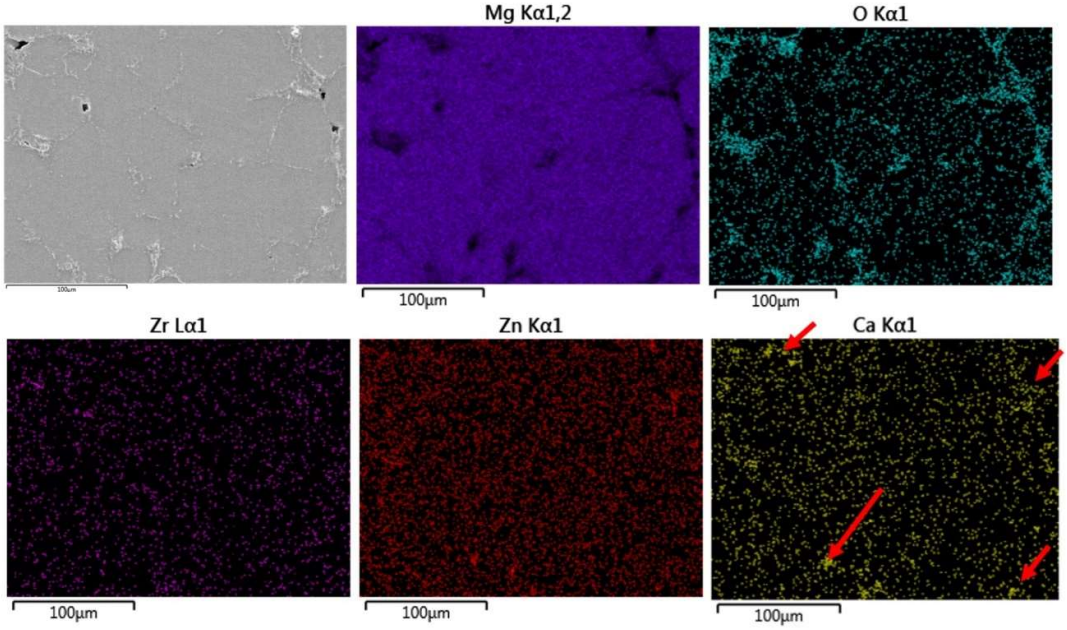

Fig. 9. The EDS element mappings of binder jet printed and sintered Mg-0.2 wt.% Ca sample.

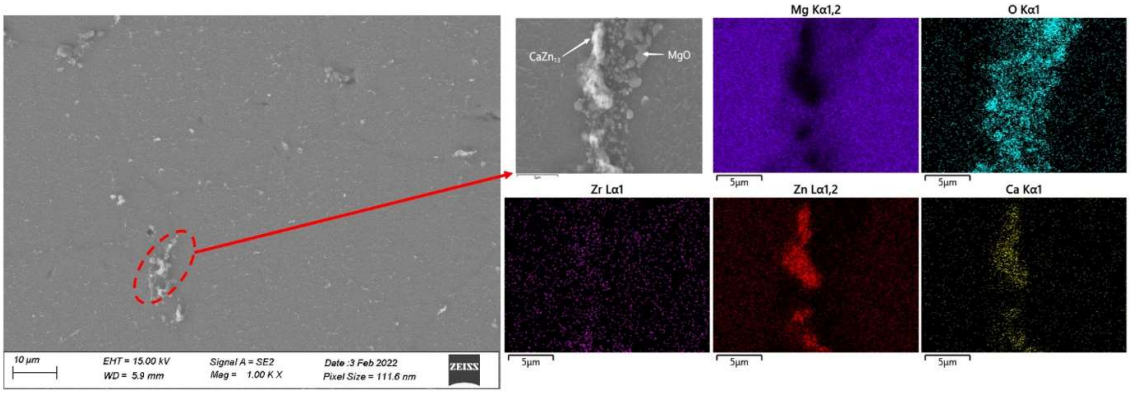

Fig. 10. The EDS element mappings at the grain boundaries of binder jet printed and sintered Mg-0.2 wt.% Ca.

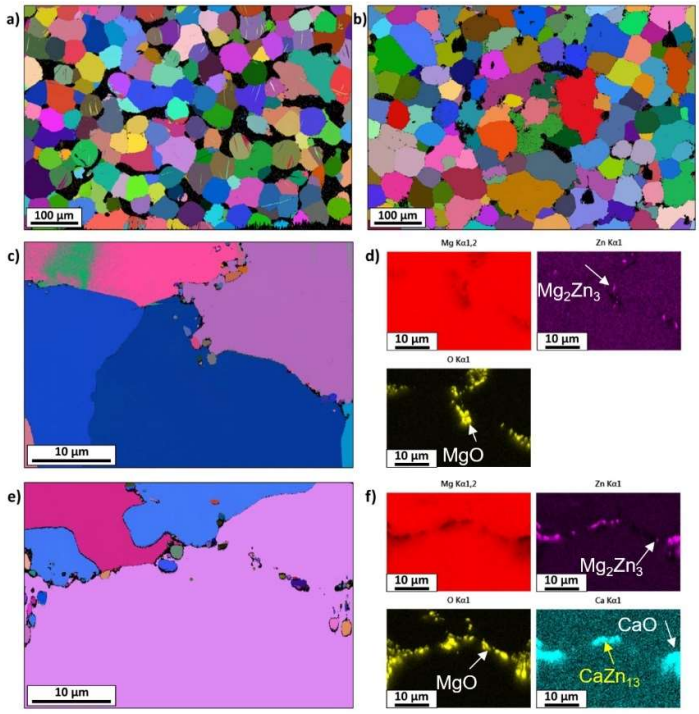

Fig. 11. The EBSD of binder jet printed and sintered samples. a) Mg, b) Mg-0.2 wt.% Ca, c) high magnification of the Mg sample focusing on the grain boundary region, d) the elemental mapping of the same area in (c), e) high magnification of Mg-0.2 wt.% Ca focusing on the grain boundary region, and f) the elemental mapping of the same area in (e).

3.2.4. Consumption mechanisms for the nanoparticle sintering aid

Fig. 12 depicts a conceptual illustration as to how the nanoparticle sintering aid results in the enhanced densification of Mg-0.2 wt.% Ca (Section 3.2.1) by putting the SEM, EDS, and EBSD results into perspective (Section 3.2.3). Our thermodynamic calculations supported by experimental results show that the Ca-based ceramic nanoparticles used as the sintering aid decompose to the elemental Ca in a solid form at ~600 °C. We previously demonstrated that

the super-solidus liquid phase sintering of Mg powder starts with bursting the Mg powder particles [14, 15]. This burst releases the liquid phase forming inside each particle and breaks its surrounding native oxide film (Fig. 12a). Regardless of where the oxide film breaks (i.e., near the interparticle region or on the surface of particles), the capillary force draws the released liquid phase together with the Ca nanoparticles to the interparticle neck regions. The solid Ca nanoparticles then dissolve in the liquid Mg phase to form Mg-Ca alloys in the sinter neck areas (Fig. 12b). According to the Mg-Ca phase diagram, up to ~5.5 wt.% of Ca is soluble in the liquid Mg phase at 615 °C and the maximum Ca solubility in solid Mg (i.e., solid solution) at 615 °C is ~0.9 wt.%. The Ca content in the molten Mg-Ca alloys reacts with the native MgO film of the Mg particles throughout the sinter neck areas (Fig. 12c). As indicated by the experimental results (Section 3.2.3), the Ca content reduced some parts of the native MgO film and not the whole MgO film covering every single Mg particle. Ca disrupts and reduces the MgO film through the following reaction:

$$MgO + Ca \rightarrow Mg + CaO \quad (5)$$

This reaction states that the total amount of oxygen remains the same in the sinter neck area but Ca takes over Mg's oxygen. This reduction is essential for the sintering kinetics of Mg powder. The diffusion rate of Mg atoms through MgO (i.e., 5.25×10^{-24} m^2/s at 650 °C) is 10^{12} times lower than the self-diffusivity rate of Mg (i.e., 3.01×10^{-12} m^2/s at 650 °C). As a result, the Ca content provides the Mg-0.2 wt.% Ca sample with enhanced kinetics to improve its sintering densification rate compared with the Mg counterpart. Meanwhile, a fraction of the Ca content from the molten Mg-Ca alloy reacts with the Zn content. $CaZn_{13}$ forms and precipitates along the grain boundaries (Fig. 12c). As sintering time continues, the molten Mg-Ca alloy diffuses from the sinter neck area to the Mg powder particles connecting through the liquid bridges (Fig. 12d). This diffusion eventually forms a solid solution Mg-Ca alloy within the Mg powder particles.

In terms of the Mg sample without the sintering aid, the presence of the oxide film hinders the coalescence of adjacent Mg powder during the sintering process. At first, the liquid phase forming in each particle breaks apart the MgO film. The MgO inclusions get transported along with the liquid phase and eventually accumulate along the grain boundaries. Hence, for the Mg sample, the sintering kinetics is primarily controlled by the thickness of the MgO film and how the film is either cracked or disrupted during the liquid phase sintering process. Therefore, the content of MgO in the primary Mg powder feedstock should remain low, and the powder particles must protect against oxygen pick-up throughout the binder jet printing and sintering processes.

According to the above mechanism and the microstructural analyses, Ca content from the sintering aid was consumed in three distinctive manners during the sintering process: 1) to react with the MgO film; 2) to react with the other alloying elements (i.e., Zn in the current study); and 3) to diffuse within the Mg particles and form a solid solution Mg-Ca. According to the Mg-Ca phase diagram, the maximum solubility of Ca in Mg in a solid solution is 1.34 wt.%. The first and second ways of Ca consumption occur in the sinter neck areas, whereas the third way involves a time-dependent diffusion of Ca from the sinter necks through a longer pathway within Mg particles. As such, it seems that the third way would depend on how much unconsumed Ca is left behind from the first and second manners of Ca consumption. We hypothesize that minimizing the Ca content to be consumed in the third way is plausible by fine-tuning the quantity of sintering aids. Thus, the undesirable compositional change imposed by adding sintering aids would be avoided or minimized. Such a targeted-nano-alloying approach would be an avenue for our future research studies.

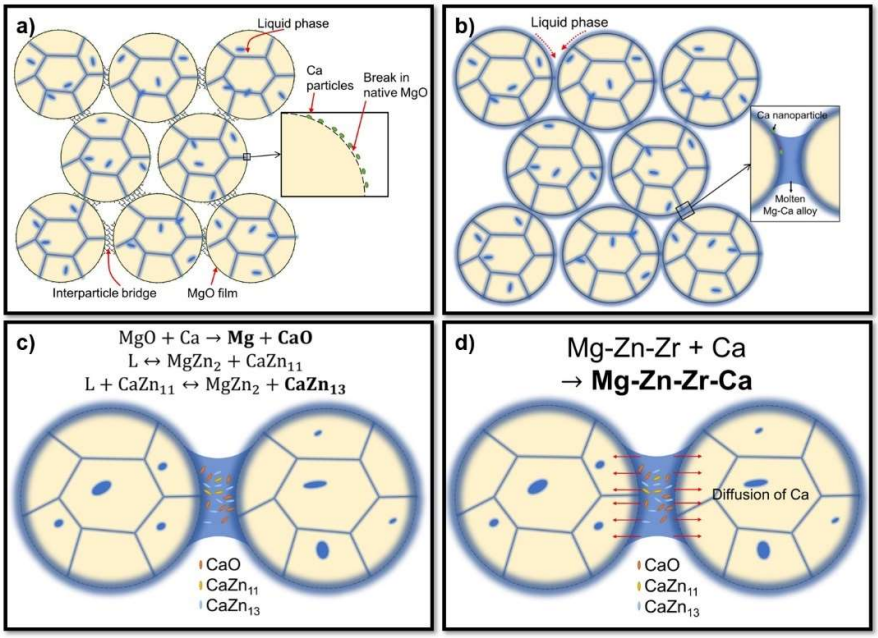

Fig. 12. Schematic representations of the super-solidus liquid phase sintering combined with the Ca-containing nanoparticles as a sintering aid for the densification of binder jet printed Mg powder. a) the formation of the liquid phase within grains and along grain boundaries during super-solidus liquid phase sintering results in breaking the native MgO film, b) the transfer of the released liquid and the solid Ca nanoparticles to sinter neck areas forms localized islands of molten Mg-Ca alloys at sinter neck areas, c) the reduction and disruption of the native MgO film and the precipitation of CaZn13 in the sinter neck areas as a result of the reactions with Ca content supplied from the localized islands of molten Mg-Ca alloy, and d) the diffusion of the molten Mg-Ca alloys into adjacent Mg powder particles forms Mg-Ca solid solutions within each powder particle.

3.2.5. Mechanical properties

Fig. 13 illustrates the results of compression and tensile tests for the Mg and Mg-0.2 wt.% Ca samples, and the corresponding mechanical properties are summarized in Table 3. Compared with the Mg sample, the tensile strength of the Mg-0.2 wt.% Ca sample was enhanced by ~30%, and more importantly, the elongation increased significantly from 2% to 5.7%. The compressive strength (i.e., ~15%) and elastic modulus (i.e., ~18%) of the Mg-0.2 wt.% also improved. As anticipated, the trend in mechanical properties is consistent with the trend in density and microstructural features. Relative density is the most influential factor determining the mechanical properties of a porous material. Among various equations in the literature for the relationship between mechanical properties and relative density, the following Gibson-Ashby model that is used in powder metallurgy can be applied as a generic model to correlate the elastic modulus and strength of a porous material with its relative density [24]:

$$P = P_s (\rho/\rho_s)^M \quad (6)$$

where P is the mechanical property of a porous material, P_s is the mechanical property of a dense material, ρ is the density of a porous material, ρ_s is the density of a dense material, and M is a proportionality constant. The exponent M represents the sensitivity of a mechanical property to porosity for a porous material. The mechanical properties of the binder jet-printed and sintered samples correlated with their relative density to determine the M values. The exponent M was found to be 2.2 for the elastic modulus, 1.93 for compressive strength, and 3.53 for tensile strength. The reason for the larger M value under tension compared to compression is associated with the densification occurring during the compression of porous structures [48]. Maconachie et al. [48] reported that the elastic modulus for various materials correlated with their relative density when the M value is 2.

Fig. 14 displays the SEM micrographs taken from the tensile fracture surface of the two samples. Fig. 14a shows the typical fracture surface of the Mg sample. As indicated by the red arrows in Fig. 14b, splitting along the sinter neck areas between Mg particles occurred in this sample. This characteristic led to a brittle fracture mode whereby several cracks formed in a tensile specimen to cause premature fracture without plastic deformation. Comparing between Fig. 14a and c revealed that larger and deeper tear ridges and dimples existed across the fracture surface of the Mg-0.2 wt.% Ca sample, indicating the characteristic of mixed brittle-ductile fracture. In contrast to the Mg sample (Fig. 14b), cleaving along sinter necks was not clearly observed in the fracture surface for the Mg-0.2 wt.% sample (Fig. 14d). Therefore, ductility increased significantly. Among mechanical properties, elongation is more sensitive to porosity [49]. Substituting the elongations for both samples (Table 3) into Eq.6, the exponent M was found to be 14.1. Porosity reduced the load-bearing area but the great sensitivity of elongation to porosity was due to the existing pores acting as local stress concentration points to initiate

and propagate cracks [50]. Fig. 14 exemplifies this sensitivity as increasing porosity changes the fracture mode to a brittle type.

Table 3 lists the mechanical properties of Mg alloys obtained in various fabrication methods. The mechanical properties achieved in this study, especially the Mg-0.2 wt.% Ca sample, fall in the range of values obtained in sintered-based AM techniques (i.e., binder jetting and extrusion-based methods), powder injection molding, and conventional casting methods of alloys with similar chemical compositions. Generally, the mechanical performance of sintered-based AM samples in particulate tensile properties is lower than those fabricated by powder bed fusion techniques due to a lower density and larger grain size. Interestingly, the tensile properties of binder-jet printed Mg-Zn-based alloys in this study exceeded the properties of denser Mg-Zn alloys fabricated by laser powder bed fusion. This is because Mg-Zn alloys tend to develop hot cracking during laser powder bed fusion. This study thus demonstrates the advantage of the binder jet process on Mg alloys over other AM methods, which have shown poor printability.

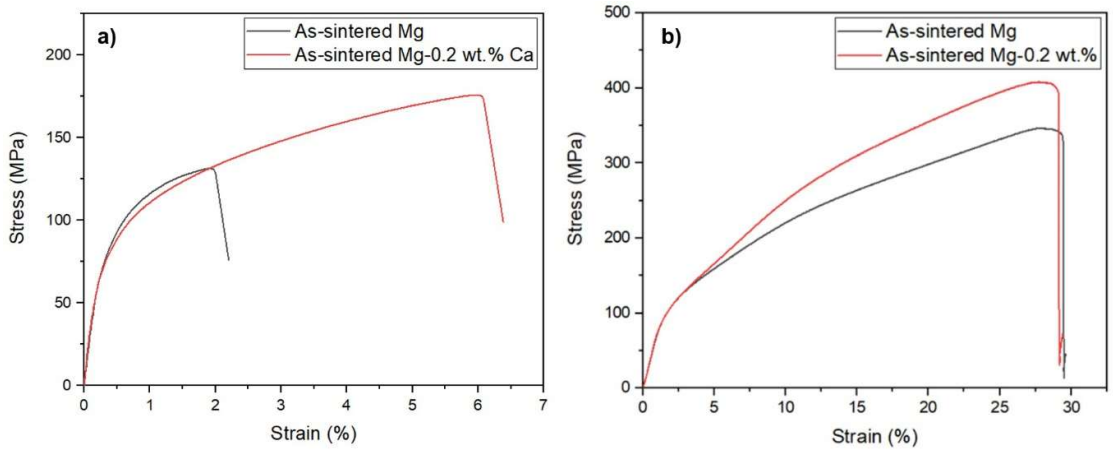

Fig. 13. Stress-strain curves for binder jet printed and sintered Mg and Mg-0.2 wt.% Ca samples under a) tension and b) compression.

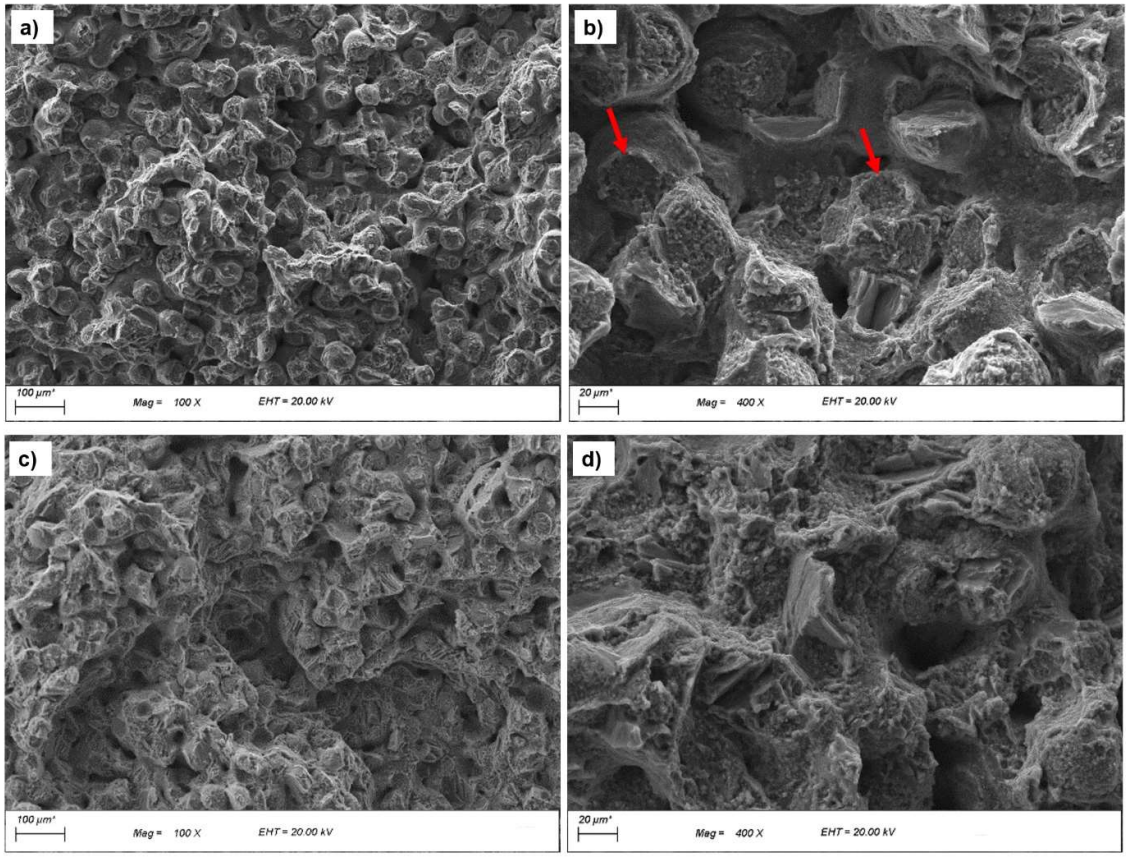

Fig. 14. SEM images of the tensile fracture surface for binder jet-printed and sintered samples. a & b) Mg, and c & d) Mg-0.2 wt.% Ca.

Table 3- Material properties of binder jet-printed and sintered Mg alloys compared to various fabrication methods.

Chemical composition	**Fabrication method**	**Density (%)**	**Grain sizes (µm)**	**Tensile properties**			**Compressive properties**		**E (GPa)**	**Ref**
				YS (MPa)	UTS (MPa)	Elongation (%)	Compressive strength (MPa)	Strain at break (%)		
Mg-5.9Zn-0.13Zr-0.2Ca	Binder jet printing and sintering	93.9 ± 0.6	47.3 ± 21.4	92.8 ±1.6	173 ± 5.3	5.7 ± 0.7	407 ± 1.6	28.1 ± 0.7	42.74 ± 0.34	This study
Mg-5.9 Zn-0.13Zr	Binder jet printing and sintering	86.8 ± 0.3	41.4 ± 15.4	101 ± 0.5	133 ± 4.0	2.0 ± 0.1	353 ± 9.1	28.5 ± 0.5	36.29 ± 0.22	This study
Mg-5.06Zn-0.15Zr	Binder jet printing and sintering at 625 °C	>92		120	159 ± 11.4	3.6 ± 0.1	371	-	39	[18]
AZ91D	Binder jet printing and complete liquid phase sintering	96.7–99.5	172–698	-	-	-	342–394	20–27	-	[23]
AZ91	Fused filament fabrication and sintering	95	-	70-79	193-207	2.4–2.8	-	-	-	[51]

Mg-0.9 wt.% Ca	Metal injection moulding and sintering	94–98	23.3	64	131	6.8		-	-	[26]
Mg-6Zn	Selective laser melting	94.7	-	-	45	1.4		-	-	[52]
Mg-4Zn	Selective laser melting	98	-	-	60	2.5		-	-	[52]
Mg-5.4Zn-0.84Zr	Laser powder bed fusion	-	7.3	-	-	-		-	-	[53]
Mg-5Zn	Casting into a permanent steel mould	-	55	75.6	195	8.5	334	-	36.47	[54]
Mg-7Zn	Casting into a permanent steel mould	-	56	67.3	135	6	353	-	36.6	[54]
Mg-5.6Zn-0.56Zr	Casting into a permanent steel mould	100	84	100	280	21.8		-	-	[55]
Mg-5.6Zn-0.56Zr-0.26Ca	Casting into a permanent steel mould	100	73	106	295	23.2		-	-	[55]

4. Conclusions

This study is the first to use Ca-containing nanoparticles as a sintering aid to successfully push the sintering densification boundaries for binder jet-printed Mg powder. Detailed analyses of the Mg feedstock containing the nanoparticles sintering aid in the as-printed and as-sintered conditions have taken the first step towards a targeted use of nanoparticles to advance printing and post-printing processes of sinter-based AM technologies for Mg alloys. The major conclusions from the current study are as follows:

1. Ca-containing nanoparticles remained intact during the binder jetting build process. In the as-printed sample, the nanoparticles either adhered to the surface of Mg particles or transferred to the interparticle bridges between Mg particles.
2. The relative density of as-printed samples descended to 49% from 54.8%, increasing the content of Ca-containing nanoparticles in the Mg feedstock from 0.2 wt.% Ca to 1.3 wt.% Ca. This reduction in the as-printed density caused the relative density of as-sintered samples to decline by 13%.

3. The addition of the Ca-containing nanoparticle improved the densification rate up to 25% when compared to the monolithic Mg counterpart. The maximum relative density of 93.5% was achieved in the Mg-0.2 wt.% Ca sample.
4. The oxygen pick-up during the whole binder jetting and sintering process was negligible. The evaporation of alloying element (i.e., Zn) and Mg matrix led to the process-induced compositional change in as-sintered samples. The observed deviations in the chemical composition of the binder jet-printed and sintered samples are much lower when compared to those reported for laser powder bed fusion of Mg powder.
5. The sintering aid is consumed in three distinctive manners during the sintering process: 1) to react with MgO film, 2) to react with the other alloying elements, and 3) to diffuse within the Mg particles. Further work is needed to apply this insight into the consumption mechanisms of nanoparticle sintering aids to develop a targeted nano-alloying approach.
6. The mechanical properties of the Mg-0.2 wt.% Ca sample improved compared to the Mg sample: tensile strength was ~30%, elongation was ~185%, compressive strength was ~15%, and an elastic modulus was ~18%. The obtained mechanical properties fall in the range reported for binder jetting, fused filament fabrication, metal injection moulding, and conventional cast alloys but far exceed those obtained in laser powder bed fusion.

Acknowledgements

The financial support from the A*STAR Structural and Metal Alloys Programme (SMAP): Work Package II with project No. A18B1b0061 is acknowledged.

References

[1] Y. Chen, J. Dou, H. Yu, C. Chen, Degradable magnesium-based alloys for biomedical applications: The role of critical alloying elements, J Biomater Appl 33(10) (2019) 1348-1372.
[2] K. Gusieva, C.H.J. Davies, J.R. Scully, N. Birbilis, Corrosion of magnesium alloys: the role of alloying, International Materials Reviews 60(3) (2015) 169-194.

[3] F. Khorashadizade, S. Abazari, M. Rajabi, H.R. Bakhsheshi-Rad, A.F. Ismail, S. Sharif, S. Ramakrishna, F. Berto, Overview of magnesium-ceramic composites: mechanical, corrosion and biological properties, Journal of Materials Research and Technology 15 (2021) 6034-6066.
[4] S. Liu, Y. Wang, M. Yarigarravesh, M. Tayyebi, M. Tayebi, Evaluation of whisker alignment and anisotropic mechanical properties of ZK60 alloy reinforced with SiCw during KOBO extrusion method, Journal of Manufacturing Processes 84 (2022) 344-356.
[5] A.A. Luo, A.K. Sachdev, D. Apelian, Alloy development and process innovations for light metals casting, Journal of Materials Processing Technology 306 (2022) 117606.
[6] Y. Zhu, K. Zhang, Z. Meng, K. Zhang, P. Hodgson, N. Birbilis, M. Weyland, H.L. Fraser, S.C.V. Lim, H. Peng, R. Yang, H. Wang, A. Huang, Ultrastrong nanotwinned titanium alloys through additive manufacturing, Nature Materials (2022).
[7] J. Suchý, L. Klakurková, O. Man, M. Remešová, M. Horynová, D. Paloušek, D. Koutný, P. Krištofová, D. Vojtěch, L. Čelko, Corrosion behaviour of WE43 magnesium alloy printed using selective laser melting in simulation body fluid solution, Journal of Manufacturing Processes 69 (2021) 556-566.
[8] Y. Guo, G. Quan, Y. Jiang, L. Ren, L. Fan, H. Pan, Formability, microstructure evolution and mechanical properties of wire arc additively manufactured AZ80M magnesium alloy using gas tungsten arc welding, Journal of Magnesium and Alloys 9(1) (2021) 192-201.
[9] S. Wlodarski, D.Z. Avery, B.C. White, C.J.T. Mason, C. Cleek, M.B. Williams, P.G. Allison, J.B. Jordon, Evaluation of Grain Refinement and Mechanical Properties of Additive Friction Stir Layer Welding of AZ31 Magnesium Alloy, Journal of Materials Engineering and Performance 30(2) (2021) 964-972.
[10] C. Su, J. Wang, H. Li, Z. You, J. Li, High strength and rapid solution Mg alloy by adding Fe element fabricated by binder jetting additive manufacturing, Journal of Manufacturing Processes 84 (2022) 652-659.
[11] K.X. Kuah, D.J. Blackwood, W.K. Ong, M. Salehi, H.L. Seet, M.L.S. Nai, S. Wijesinghe, Analysis of the corrosion performance of binder jet additive manufactured magnesium alloys for biomedical applications, Journal of Magnesium and Alloys 10(5) (2022) 1296-1310.
[12] M. Salehi, S. Maleksaeedi, M.L.S. Nai, M. Gupta, Towards additive manufacturing of magnesium alloys through integration of binderless 3D printing and rapid microwave sintering, Additive Manufacturing 29 (2019) 100790.
[13] M. Salehi, S. Maleksaeedi, S.M.L. Nai, G.K. Meenashisundaram, M.H. Goh, M. Gupta, A paradigm shift towards compositionally zero-sum binderless 3D printing of magnesium alloys via capillary-mediated bridging, Acta Materialia 165 (2019) 294-306.
[14] M. Salehi, S. Maleksaeedi, M.A.B. Sapari, M.L.S. Nai, G.K. Meenashisundaram, M. Gupta, Additive manufacturing of magnesium–zinc–zirconium (ZK) alloys via capillary-mediated binderless three-dimensional printing, Materials & Design 169 (2019) 107683.
[15] M. Salehi, H.L. Seet, M. Gupta, H. Farnoush, S. Maleksaeedi, M.L.S. Nai, Rapid densification of additive manufactured magnesium alloys via microwave sintering, Additive Manufacturing 37 (2021) 101655.
[16] J. Dong, Y. Li, P. Lin, M.A. Leeflang, S. van Asperen, K. Yu, N. Tümer, B. Norder, A.A. Zadpoor, J. Zhou, Solvent-cast 3D printing of magnesium scaffolds, Acta Biomaterialia 114 (2020) 497-514.
[17] N. Kleger, M. Cihova, K. Masania, A.R. Studart, J.F. Löffler, 3D Printing of Salt as a Template for Magnesium with Structured Porosity, Advanced Materials 31(37) (2019) 1903783.
[18] Z. Zeng, M. Salehi, A. Kopp, S. Xu, M. Esmaily, N. Birbilis, Recent progress and perspectives in additive manufacturing of magnesium alloys, Journal of Magnesium and Alloys 10(6) (2022) 1511-1541.

[19] P.J. Burke, Z. Bayindir, G.J. Kipouros, X-ray photoelectron spectroscopy (XPS) investigation of the surface film on magnesium powders, Appl Spectrosc 66(5) (2012) 510-8.
[20] M. Salehi, S. Maleksaeedi, H. Farnoush, M.L.S. Nai, G.K. Meenashisundaram, M. Gupta, An investigation into interaction between magnesium powder and Ar gas: Implications for selective laser melting of magnesium, Powder Technology 333 (2018) 252-261.
[21] K.X. Kuah, M. Salehi, W.K. Ong, H.L. Seet, M.L.S. Nai, S. Wijesinghe, D.J. Blackwood, Insights into the influence of oxide inclusions on corrosion performance of additive manufactured magnesium alloys, npj Materials Degradation 6(1) (2022) 36.
[22] M. Esmaily, Z. Zeng, A.N. Mortazavi, A. Gullino, S. Choudhary, T. Derra, F. Benn, F. D'Elia, M. Müther, S. Thomas, A. Huang, A. Allanore, A. Kopp, N. Birbilis, A detailed microstructural and corrosion analysis of magnesium alloy WE43 manufactured by selective laser melting, Additive Manufacturing 35 (2020) 101321.
[23] C. Su, J. Wang, H. Li, Z. You, J. Li, Binder-jetting additive manufacturing of Mg alloy densified by two-step sintering process, Journal of Manufacturing Processes 72 (2021) 71-79.
[24] R.M. German, Sintering: from Empirical Observations to Scientific Principles, Butterworth-Heinemann, Boston, 2014.
[25] M. Wolff, T. Ebel, M. Dahms, Sintering of Magnesium, Advanced Engineering Materials 12(9) (2010) 829-836.
[26] M. Wolff, J.G. Schaper, M. Dahms, T. Ebel, K.U. Kainer, T. Klassen, Magnesium powder injection moulding for biomedical application, Powder Metallurgy 57(5) (2014) 331-340.
[27] M. Wolff, J.G. Schaper, M.R. Suckert, M. Dahms, T. Ebel, R. Willumeit-Römer, T. Klassen, Magnesium Powder Injection Molding (MIM) of Orthopedic Implants for Biomedical Applications, JOM 68(4) (2016) 1191-1197.
[28] M. Salehi, M. Gupta, S. Maleksaeedi, M.L.S. Nai, Inkjet Based 3D Additive Manufacturing of Metals, Materials Research Forum LLC, Millersville, PA, USA, 2018.
[29] M. Jönsson, D. Persson, D. Thierry, Corrosion product formation during NaCl induced atmospheric corrosion of magnesium alloy AZ91D, Corrosion Science 49(3) (2007) 1540-1558.
[30] A. Entezari Zarandi, F. Larachi, G. Beaudoin, B. Plante, M. Sciortino, Nesquehonite as a carbon sink in ambient mineral carbonation of ultramafic mining wastes, Chemical Engineering Journal 314 (2017) 160-168.
[31] R.L. Frost, S.J. Palmer, Infrared and infrared emission spectroscopy of nesquehonite Mg(OH)(HCO3)·2H2O–implications for the formula of nesquehonite, Spectrochimica Acta Part A: Molecular and Biomolecular Spectroscopy 78(4) (2011) 1255-1260.
[32] X. Wang, L. Andrews, Infrared Spectra of Magnesium Hydride Molecules, Complexes, and Solid Magnesium Dihydride, The Journal of Physical Chemistry A 108(52) (2004) 11511-11520.
[33] M. Barawi, C. Granero, P. Díaz-Chao, C.V. Manzano, M. Martin-Gonzalez, D. Jimenez-Rey, I.J. Ferrer, J.R. Ares, J.F. Fernández, C. Sánchez, Thermal decomposition of non-catalysed MgH2 films, International Journal of Hydrogen Energy 39(18) (2014) 9865-9870.
[34] Q. Zhang, Y. Huang, L. Xu, L. Zang, H. Guo, L. Jiao, H. Yuan, Y. Wang, Highly Dispersed MgH2 Nanoparticle–Graphene Nanosheet Composites for Hydrogen Storage, ACS Applied Nano Materials 2(6) (2019) 3828-3835.
[35] L.-X. Li, D. Xu, X.-Q. Li, W.-C. Liu, Y. Jia, Excellent fluoride removal properties of porous hollow MgO microspheres, New Journal of Chemistry 38(11) (2014) 5445-5452.
[36] K.J. Fricker, A.-H.A. Park, Effect of H2O on Mg(OH)2 carbonation pathways for combined CO2 capture and storage, Chemical Engineering Science 100 (2013) 332-341.
[37] A.K. Sharma, A. Kvit, J. Narayan, Growth of single crystal MgO on TiN/Si heterostructure by pulsed laser deposition, Journal of Vacuum Science & Technology A 17(6) (1999) 3393-3396.

[38] M.C. Hales, R.L. Frost, W.N. Martens, Thermo-Raman spectroscopy of synthetic nesquehonite — implication for the geosequestration of greenhouse gases, Journal of Raman Spectroscopy 39(9) (2008) 1141-1149.
[39] J.R. Santisteban, G.J. Cuello, J. Dawidowski, A. Fainstein, H.A. Peretti, A. Ivanov, F.J. Bermejo, Vibrational spectrum of magnesium hydride, Physical Review B 62(1) (2000) 37-40.
[40] L. Matović, N. Novaković, S. Kurko, M. Šiljegović, B. Matović, Z. Kačarević Popović, N. Romčević, N. Ivanović, J. Grbović Novaković, Structural destabilisation of MgH2 obtained by heavy ion irradiation, International Journal of Hydrogen Energy 34(17) (2009) 7275-7282.
[41] Y. Liu, R. Tandon, R.M. German, Modeling of supersolidus liquid phase sintering: I. Capillary force, Metallurgical and Materials Transactions A 26(9) (1995) 2415-2422.
[42] J. Liu, A.L. Cardamone, R.M. German, Estimation of capillary pressure in liquid phase sintering, Powder Metallurgy 44(4) (2001) 317-324.
[43] C. Shuai, Y. Yang, P. Wu, X. Lin, Y. Liu, Y. Zhou, P. Feng, X. Liu, S. Peng, Laser rapid solidification improves corrosion behavior of Mg-Zn-Zr alloy, Journal of Alloys and Compounds 691 (2017) 961-969.
[44] K. Wei, Z. Wang, X. Zeng, Influence of element vaporization on formability, composition, microstructure, and mechanical performance of the selective laser melted Mg–Zn–Zr components, Materials Letters 156 (2015) 187-190.
[45] F. Attarzadeh, E. Asadi, Analysis of element loss, densification, and defects in laser-based powder-bed fusion of magnesium alloy WE43, Journal of Magnesium and Alloys 10(8) (2022) 2118-2136.
[46] S. Wasiur-Rahman, M. Medraj, Critical assessment and thermodynamic modeling of the binary Mg–Zn, Ca–Zn and ternary Mg–Ca–Zn systems, Intermetallics 17(10) (2009) 847-864.
[47] N. Yang, N. Balasubramani, J. Venezuela, S. Almathami, C. Wen, M. Dargusch, The influence of Ca and Cu additions on the microstructure, mechanical and degradation properties of Zn–Ca–Cu alloys for absorbable wound closure device applications, Bioactive Materials 6(5) (2021) 1436-1451.
[48] T. Maconachie, M. Leary, B. Lozanovski, X. Zhang, M. Qian, O. Faruque, M. Brandt, SLM lattice structures: Properties, performance, applications and challenges, Materials & Design 183 (2019) 108137.
[49] S. Wang, J. Ning, L. Zhu, Z. Yang, W. Yan, Y. Dun, P. Xue, P. Xu, S. Bose, A. Bandyopadhyay, Role of porosity defects in metal 3D printing: Formation mechanisms, impacts on properties and mitigation strategies, Materials Today (2022).
[50] S. Wang, J. Ning, L. Zhu, Z. Yang, W. Yan, Y. Dun, P. Xue, P. Xu, S. Bose, A. Bandyopadhyay, Role of porosity defects in metal 3D printing: Formation mechanisms, impacts on properties and mitigation strategies, Materials Today 59 (2022) 133-160.
[51] A.S. Vishwanath, K. Rane, J. Schaper, M. Strano, R. Casati, Rapid production of AZ91 Mg alloy by extrusion based additive manufacturing process, Powder Metallurgy 64(5) (2021) 370-377.
[52] K. Wei, X. Zeng, Z. Wang, J. Deng, M. Liu, G. Huang, X. Yuan, Selective laser melting of Mg-Zn binary alloys: Effects of Zn content on densification behavior, microstructure, and mechanical property, Materials Science and Engineering: A 756 (2019) 226-236.
[53] J. Liang, Z. Lei, Y. Chen, W. Fu, X. Chen, S. Ma, Elimination of extraordinarily high cracking susceptibility of ZK60 Mg alloy fabricated by laser powder bed fusion, Materials Letters 312 (2022) 131731.
[54] S. Cai, T. Lei, N. Li, F. Feng, Effects of Zn on microstructure, mechanical properties and corrosion behavior of Mg–Zn alloys, Materials Science and Engineering: C 32(8) (2012) 2570-2577.

[55] W. Fu, H. Yang, T. Li, J. Sun, S. Guo, D. Fang, W. Qin, X. Ding, Y. Gao, J. Sun, Enhancing corrosion resistance of ZK60 magnesium alloys via Ca microalloying: The impact of nanoscale precipitates, Journal of Magnesium and Alloys (2022).